



Ferro- vs. antiferromagnetic exchange between two Ni(II) ions in a series of Schiff base heterometallic complexes: what makes the difference?

Journal:	<i>Dalton Transactions</i>
Manuscript ID	DT-ART-11-2020-003957.R1
Article Type:	Paper
Date Submitted by the Author:	19-Jan-2021
Complete List of Authors:	Vassilyeva, Olga; Taras Shevchenko National University of Kyiv, Chemistry Buvaylo, Elena; Taras Shevchenko National University of Kyiv Kokozay, Vladimir; Taras Shevchenko National University of Kyiv Skelton, Brian; The University of Western Australia, School of Biomedical, Biomolecular and Chemical Sciences Sobolev, Alexandre; The University of Western Australia, School of Biomedical, Biomolecular and Chemical Sciences Bieńko, Alina; University of Wrocław, Faculty of Chemistry Ozarowski, Andrew; Florida State University, National High Magnetic Field Laboratory

ARTICLE

Ferro- vs. antiferromagnetic exchange between two Ni(II) ions in a series of Schiff base heterometallic complexes: what makes the difference?

Received 00th January 20xx,
Accepted 00th January 20xx

DOI: 10.1039/x0xx00000x

Olga Yu. Vassilyeva,^{*a} Elena A. Buvaylo,^a Vladimir N. Kozozay,^a Brian W. Skelton,^b Alexandre N. Sobolev,^b Alina Bieńko,^c and Andrew Ozarowski^{*d}

Three new Ni^{II}/Zn^{II} heterometallics, [NiZnL'₂(OMe)Cl]₂ (**1**), [NiZnL''(Dea)Cl]₂·2DMF (**2**) and [Ni₂(H₃L''')₂(*o*-Van)(MeOH)₂Cl·[ZnCl₂(H₄L''')](MeOH)]·2MeOH (**3**), containing three-dentate Schiff bases as well as methanol or diethanolamine (H₂Dea) or *o*-vanillin (*o*-VanH), all deprotonated, as bridging ligands were synthesized and structurally characterized. The Schiff base ligands were produced in situ from *o*-VanH and CH₃NH₂ (HL'), or NH₂OH (HL''), or 2-amino-2-hydroxymethyl-propane-1,3-diol (H₄L'''); a zerovalent metal (Ni and Zn in **1**, Zn only in **2** and **3**) was employed as a source of metal ions. The first two complexes are dimers with a Ni₂ZnO₆ central core, while the third compound is a novel heterometallic cocrystal salt solvate built of a neutral zwitterionic Zn^{II} Schiff base complex and of ionic salt containing dinuclear Ni^{II} complex cations. The crystal structures contain either centrosymmetric (**1** and **2**) or non-symmetric di-nickel fragment (**3**) with Ni...Ni distances in the range 3.146–3.33 Å. The exchange coupling is antiferromagnetic for **1**, $J = 7.7 \text{ cm}^{-1}$, and ferromagnetic for **2**, $J = -6.5 \text{ cm}^{-1}$ (using the exchange Hamiltonian in a form $\hat{H} = J\hat{S}_1\hat{S}_2$). The exchange interactions in **1** and **2** are comparable to the zero-field splitting (ZFS). High-field EPR revealed moderate magnetic anisotropy of opposite signs: $D = 2.27 \text{ cm}^{-1}$, $E = 0.243 \text{ cm}^{-1}$ (**1**) and $D = -4.491 \text{ cm}^{-1}$, $E = -0.684 \text{ cm}^{-1}$ (**2**). Compound **3** stands alone with very weak ferromagnetism ($J = -0.6 \text{ cm}^{-1}$) and much stronger magnetic anisotropy with $D = -11.398 \text{ cm}^{-1}$ and $E = -1.151 \text{ cm}^{-1}$. Attempts to calculate theoretically the exchange coupling (using the DFT "broken symmetry" method) and ZFS parameters (with the *ab-initio* CASSCF method) were successful in predicting the trends of J and D among the three complexes, while the quantitative results were less good for **1** and **3**.

Introduction

Polynuclear complexes of paramagnetic metals are appealing research objects from two large areas of scientific interest – bioinorganic and materials chemistry. Many natural metalloenzymes have been found to contain dinuclear or polynuclear active sites.¹ Examples among Ni-based enzymes include urease with a dinickel centre, which hydrolyses urea into carbon dioxide and ammonia, and NiFe hydrogenase, which catalyzes the reversible two-electron reduction of protons to H₂.² GloA2, a Zn inactive glyoxalase from *Pseudomonas aeruginosa*, can accommodate two distinct metal-binding arrangements simultaneously, each of which catalyzes a different reaction.³ One active site contains a single activating

Ni²⁺ ion, whereas the other contains two inactivating Zn²⁺ ions. In addition to its glyoxalase I activity, the enzyme can function as a Zn²⁺/Co²⁺-dependent hydrolase. Metal complexes of bioinspired ligands that mimic the catalytic effect of natural enzymes help to elucidate the enzymatic reaction mechanisms and may have practical applications, e.g., for the design of low molecular weight synthetic catalysts.⁴

Molecular systems with a magnetic core of transition metal ions surrounded by organic ligands have shown interesting and valuable properties such as single-molecule magnet (SMM) behavior for the promising applications in materials chemistry.⁵ The Ni compounds that contributed to the field range from Ni(I) and Ni(II) mononuclear complexes⁶ to the [Ni₁₂] cycle [Ni₁₂(chp)₁₂(O₂CMe)₁₂(thf)₆(H₂O)₆] (chp – 6-chloro-2-pyridonate)⁷ and a giant [Ni₂₁] spin cluster anion, [Ni₂₁(cit)₁₂(OH)₁₀(H₂O)₁₀]¹⁶⁻ (H₄cit = citric acid).⁸ The dinuclear complexes shown to behave as SMMs were discovered in the families of heterometallic Ni^{II}Ln^{III} species (Ln = Eu, Gd, Tb, Ho, Er, Y).⁹

These findings motivated our investigation of a series of polynuclear heterometallic Ni/Zn complexes, [NiZnL'₂(OMe)Cl]₂ (**1**), [NiZnL''(Dea)Cl]₂·2DMF (**2**) and [Ni₂(H₃L''')₂(*o*-Van)(MeOH)₂Cl·[ZnCl₂(H₄L''')](MeOH)]·2MeOH (**3**), containing Schiff base ligands derived from 2-hydroxy-3-methoxybenzaldehyde (*o*-vanillin, *o*-VanH) and CH₃NH₂ (HL'), or NH₂OH

^a Department of Chemistry, Taras Shevchenko National University of Kyiv, 64/13 Volodymyrska str., Kyiv 01601, Ukraine.

^b School of Molecular Sciences, M310, University of Western Australia, Perth, WA 6009, Australia.

^c Faculty of Chemistry, University of Wrocław, F. Joliot-Curie 14, Wrocław 50-383, Poland.

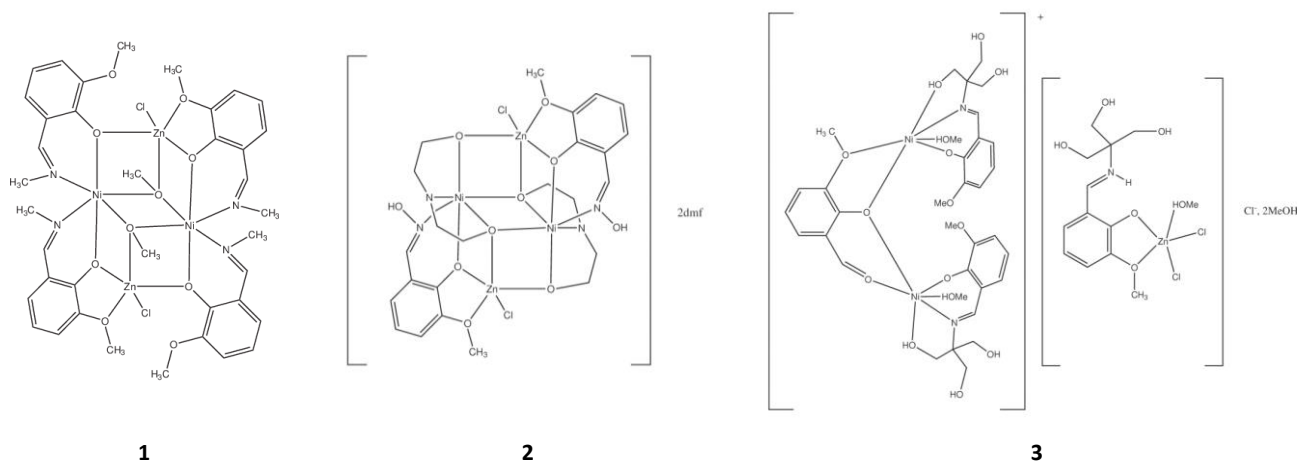
^d National High Magnetic Field Laboratory, Florida State University, 1800 East Paul Dirac Drive, Tallahassee, Florida 32310

Electronic Supplementary Information (ESI) available: IR spectra, crystallographic details, magnetic details, and computational details. CCDC 1898551, 1898552 and 1837991. For ESI and crystallographic data in CIF or other electronic format see DOI: 10.1039/x0xx00000x

(HL''), or 2-amino-2-hydroxymethyl-propane-1,3-diol (tris, H₄L'''), respectively (Scheme 1, H₂Dea – diethanolamine, DMF – N,N-dimethylformamide).

By using our previous experience in applying zerovalent metals to prepare heterometallic complexes of diverse potential advantages,¹⁰ **1–3** have been facily synthesized from the reactions of the pre-formed Schiff base ligands, Zn powder and NiCl₂·6H₂O (and Ni powder in the case of **1**) in non-aqueous

media. The first two complexes are centrosymmetric dimers with a Ni₂Zn₂O₆ central core of a defect dicubane-like topology with two missing vertices. The phenoxo-bridging from the Schiff base ligands ensures formation of the [NiZn] heterometallic moieties, which further dimerize into tetranuclear assemblies through alkoxo-bridges from methoxide (**1**) and aminoalcohol anions (**2**).



Scheme 1. Structural formulas of [NiZnL'₂(OMe)Cl]₂ (**1**), [NiZn''(Dea)Cl]₂·2DMF (**2**) and [Ni₂(H₃L''')₂(o-Van)(MeOH)₂]Cl·[ZnCl₂(H₄L''')(MeOH)]·2MeOH (**3**).

In the third compound, the cocrystallization of zwitterionic Schiff base complex [ZnCl₂(H₄L''')(MeOH)], nickel ionic salt with asymmetric dinuclear complex cation, [Ni₂(H₃L''')₂(o-Van)(MeOH)₂]Cl, and methanol molecules has occurred. A growing number of multicomponent crystal structures present in the Cambridge Structural Database prompted a new classification of them into seven subclasses based on the residue types (solvent, ion, cofomer) in the crystal: true solvates, true salts, true cocrystals, salt solvates, cocrystal solvates, cocrystal salts, and cocrystal salt solvates.¹¹ Within the three latter subclasses, heterometallic systems derived from 3-R-salicylaldehyde-diamine (R = methoxy-, ethoxy-) ligands have been extensively explored.¹² This particular ligand family possesses a O(phenoxo)₂O(R-O)₂ compartment able to interact with cations (H₃O⁺,^{12a} NH₄⁺,^{12b,c} alkylenediammonium^{12d,e}) or solvent molecules^{12f} due to the formation of bifurcated hydrogen bonds, which stabilize rare examples of the self-assembled two- to four-component cocrystals of metal complexes. At the same time, this characteristic feature seems to restrict the structural diversity of the resulting multicomponent crystals to 0-D and 1-D arrangements. According to the suggested classification, the multicomponent system **3** which is built of alternating sheets of a neutral Zn^{II} complex, ionic Ni^{II} salt and solvent molecules is a novel 2-D heterometallic cocrystal salt solvate.

Understanding the electronic structure of the metal core of the polymetallic species gives insights into chemical transformations it may perform. In the class of systems with enhanced magnetic anisotropy, this type of information can be obtained through combination of solid-state magnetic

measurements and high-frequency and -field electron paramagnetic resonance (HF-EPR) spectroscopy.¹³ Dimeric molecules are particularly useful models for studying the coupling mechanisms between two paramagnetic ions.¹⁴ Magnetic susceptibility measurements revealed antiferromagnetic (**1**) and ferromagnetic coupling (**2**) between the Ni centres, while **3** seemed to exhibit no significant metal–metal interaction. The determination of exchange and dipole–dipole contributions to the zero–field splitting (ZFS) characterizing the excited states of the dimers and binuclear cation was achieved using HF-EPR technique as a function of different frequencies and temperatures.

Results and discussion

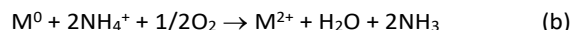
Synthetic aspects

The title compounds have been synthesized as part of the ongoing research on Schiff base metal complexes aimed at the preparation and investigation of heterometallic compounds of various compositions and structures. In these studies, the synthetic strategy, *direct synthesis*, based on the interaction of a fine metal powder (M₁⁰) with a salt of another metal (M_{II}X_n) in non-aqueous solution of Schiff base ligand (HL), in air, is successfully employed¹⁰ as shown in the general scheme:



The background to such a synthetic scheme was established in our earlier investigations of the open-air reactions of metal powders (Cu⁰, Ni⁰, Zn⁰) with ammonium salts and N/O-

containing organic ligands to produce monometallic coordination compounds.^{15a-c} It was shown that zerovalent metal oxidation and complex formation is due to the presence of a proton-donating agent (NH₄X) and dioxygen from the air. The latter is reduced to give H₂O as summarised in the following reaction scheme:



An ammonium salt also supplies required anions. With use of other proton-donating agents (aminoalcohols, Schiff bases) the developed synthetic route evolved in the preparation of heterometallic complexes by scheme (a).

In the present study, the ligands HL', HL'' and H₄L''' were synthesized in situ by condensation of *o*-vanillin and CH₃NH₂·HCl, NH₂OH·HCl, or tris, respectively, in non-aqueous solvents in the presence of diethanolamine (in the case of **1** and **2**) used as a basic agent. The condensation reactions were utilized without isolation of the resulting Schiff base. The heterometallic complex **1** was prepared using a combination of the schemes (a) and (b). Zn and Ni powders easily dissolved in the ethanol solution of an ammonium salt and preformed HL' under mild heating and magnetic stirring in open air. Evaporation of the resultant solution to dryness and redissolving the residue in methanol facilitated deposition of single crystals of **1** suitable for X-ray crystallography. In the case of HL'', the use of zerovalent zinc, nickel(II) chloride hexahydrate and diethanolamine afforded the mixed-ligand dimer **2** in which deprotonated diethanolamine molecules provided additional alkoxo-bridges between metal centres. Deprotonation of aminoalcohols in reactions employing zerovalent metals to synthesize heterometallic complexes was established by some of us earlier.^{15d,e}

The third compound was prepared without addition of a basic agent. As we found before, commonly used triethylamine promoted crystallization of the individual components in the case of Zn⁰-MnCl₂^{16a} and Cu⁰-Zn(CH₃COO)₂^{16b} systems with H₄L'''. Crystal structures of about 30 metal complexes of H₄L''' found in the Cambridge Database mostly comprise polynuclear

homo- Co^{II}Co^{III}, V₂, Cu₄, Mn₄, Ni₄, Ln₉ and Ln₁₀ and heterometallic 1s-3d and 3d-4f assemblies of 4-20 nuclearity. Obviously, the Schiff base ligand favours formation of paramagnetic clusters due to the presence of the tripodal alcohol functionality. At the same time, the lack of heterometallic structures with two kinds of 3d metal ions supported by H₄L''' is also evident. In the present work, slow evaporation of the green solution resulted from the interaction of zinc powder and NiCl₂ hexahydrate with tris and *o*-vanillin in methanol led to the cocrystallization of the nickel- and zinc-containing cofomers in an appreciable yield. Their formation seem to be conditioned by the incomplete condensation that left some *o*-vanillin unreacted and the displacement of the proton from the phenolic oxygen to the imine nitrogen atom which produced zwitterionic form of H₄L''' upon complexation (see below).

Crystal structures

[NiZnL'(OMe)Cl]₂ (1) and **[NiZnL''(Dea)Cl]₂·2DMF (2)**. Complexes **1** and **2** are built of electroneutral molecules that consist of two zinc(II) and two nickel(II) atoms, two (**2**) or four Schiff base ligands deprotonated at the phenol O atoms (**1**), two methoxide (**1**) or two doubly deprotonated aminoalkoxo groups (**2**) and two chlorine ions in a centrosymmetric arrangement (Figure 1). There are also DMF molecules of crystallization in the crystal structure of **2**. Both complexes possess a defect dicubane-like {Ni₂Zn₂O₆}²⁺ core in which two vertices are missing. The nickel coordination environments, NiN₂O₄, in the two complexes are distorted octahedral with very close geometric parameters: Ni-N and Ni-O bond lengths fall in the ranges 2.0364(13)-2.1128(13) and 2.019(2)-2.097(2) Å, respectively. The *cis* angles at the nickel atom in **1** vary from 79.47(8) to 96.98(8), the *trans* angles are equal to 166.71(10)-174.91(9)° (Table S1). The nickel octahedron in **2** is more distorted as evidenced by the *cis* angles at the metal atom varying from 80.34(4) to 106.32(4) and the *trans* angles being equal to 153.77(4)-172.53(4)° (Table S1).

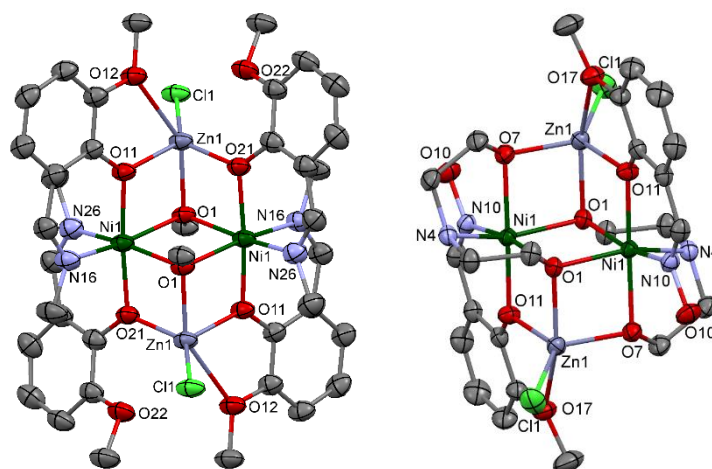
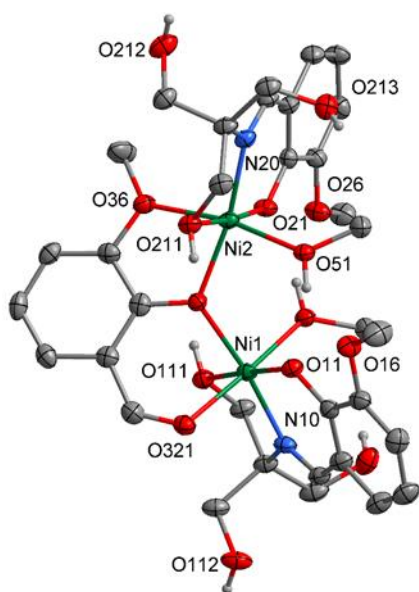


Figure 1. Molecular structures and principal atom labeling of **1** (left) and **2** (right). Displacement ellipsoids for non-H atoms are drawn at the 50% probability level. H atoms are not shown.

The zinc atoms in **1** and **2** have three quite short bonds with oxygen atoms of the Schiff bases, methoxide ion or deprotonated diethanolamine moieties [Zn–O: 1.9599(11)–2.0980(18) Å] and a longer bonding distance to the chlorine atom Cl(1) [**1**: 2.2763(8), **2**: 2.2106(5) Å] in a severely distorted tetrahedral geometry [\angle : 80.23(8)–133.36(6)°] (Table S1). An additional weak contact to the oxygen atom of the methoxy group of the Schiff base ligands, O(12) and O(17), at 2.477(2) (**1**) and 2.3674(11) Å (**2**) transforms the Zn(1) coordination spheres into an irregular square pyramid with chlorine atom in the apex. The values of the angular structural parameter τ are 0.25 and 0.40 for **1** and **2**, respectively. The phenoxo-, methoxide- or aminoalkoxo-bridges between metal centres result in the Ni...Ni separations of about 3.220 (**1**) and 3.146 Å (**2**). The Ni...Zn distances for both complexes are in the range 3.031–3.143 Å.

The heterometallic molecules show no significant intermolecular contacts in the solid state. Classical hydrogen-bonding interactions are absent. Layers of dimers are stacked parallel to the *ab* plane, with the minimum Ni...Ni distances being approximately 9.722 (**1**) and 8.810 (**2**) Å inside a layer, and with minimum distances between the nickel atoms from the two consecutive layers being equal to 11.019 (**1**) and 11.188 (**2**) Å (Figure S1). In **2**, solvent DMF molecules reside between the layers.

[Ni₂(H₃L^{'''})₂(*o*-Van)(MeOH)₂Cl·[ZnCl₂(H₄L^{'''})(MeOH)]·2MeOH (**3**). Ni atoms in the dinuclear complex cation are octahedral with the coordination spheres each consisting of one phenolate oxygen atom, the oxygen of the methyl group and one hydroxyl group of the deprotonated H₃L^{'''} ligands, one methanol molecule, the phenolate oxygen atom of the deprotonated *o*-Van⁻ ligand, and either the aldehyde oxygen atom [for Ni(1)] or the methoxy oxygen atom [for Ni(2)] of the *o*-Van⁻ ligand (Figure



2 top).

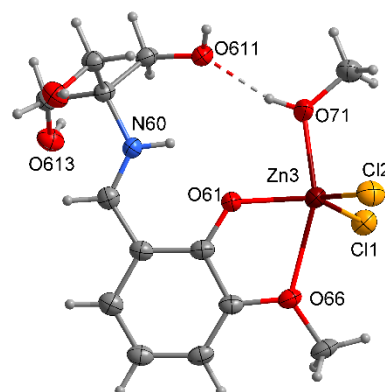


Figure 2. Molecular structures and atom labeling in the dinuclear nickel cation (top) and neutral Schiff base zinc complex of **3** (bottom) with ellipsoids at the 30% probability level. CH hydrogen atoms in the cation have been omitted for clarity.

The Ni–N/O distances vary from 1.989(3) to 2.096(3) Å with the Ni(2) bond to the methoxy oxygen atom of the *o*-Van⁻ being slightly longer [2.153(3) Å] (Table S2). Both octahedra are fairly distorted as evidenced by the *cis* and *trans* angles at the metal atoms in the ranges 76.28(11)–97.64(13) and 168.62(12)–176.34(12)°, respectively. The phenoxo-bridged nickel atoms are separated at 3.33 Å. The cations are further stabilised by intramolecular hydrogen bonds with participation of coordinated (O41, O51) and non-coordinated (O91) methanol molecules (Figure 2 top, Table S3).

The species containing the Zn atom contains one neutral H₄L ligand bound to the metal centre through the phenolate and methoxy oxygen atoms (Figure 2 bottom). H₄L ligand is protonated, not at the oxygen atom, but at the imine nitrogen atom. The coordination sphere is completed by one molecule of methanol (O71) and two chloride ions (Cl1 and Cl2). The coordination sphere of the Zn atom can be described as distorted trigonal bipyramidal with the two Cl atoms and the phenolate oxygen atom forming the central plane and the axial atoms being the methoxy oxygen atom and the methanol molecule. The metal distance to the methoxy oxygen atom, Zn(3)–O(66) 2.425(3) Å, is significantly longer than those to the other ligands; the mean of the two other Zn–O and two Zn–Cl bond distances are equal to 2.022 and 2.251 Å, respectively (Table S2). The intramolecular N–H...O and O–H...O hydrogen-bond interactions of 2.620(5) and 2.666(5) Å in the Zn molecule strengthen an almost planar conformation of its skeleton (Table S3).

The nickel cations are joined by strong O–H...O bonds between their sticking “out” OH⁻ groups to form sheets parallel to the *bc* plane. These alternate with sheets made of the zwitterionic Zn-containing molecules (Figure 3). The chloride anion forms three hydrogen bonds with the hydroxy groups of the tris fragments of the Schiff base ligands from nickel and zinc co-formers to adopt a T-shaped geometry (Figure S2). The T-shape of the hydrogen bonding to the Cl3 atom reflects primarily the requirements of the chloride ion to satisfy a coordination number of 3 in hydrogen bonding environments.¹⁷ The geometrical placement of hydrogen bonds imposed by the

T-shaped geometry of the anion is apparently responsible for the layered packing pattern of **3** in the solid state.

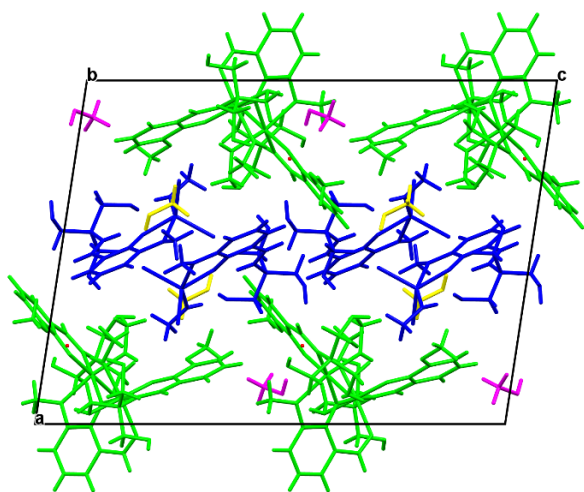


Figure 3. Crystal packing of **3** viewed along *b*, showing alternating layers of ionic Ni species (green) and neutral Zn species (blue). Chloride anions are given as red circles; non-coordinated methanol molecules are shown in pink and yellow in different layers.

High-Field EPR spectra and their interpretation

The three complexes presented quite different spectra indicative of large differences in their ZFS parameters (Figure 4). The general spin Hamiltonian (1) appropriate for our di-nickel systems consists of a part related to the interactions between the two nickel ions, expressed by terms with J , D_{12} and E_{12} , a part related to ZFS on individual metal ions, expressed by terms with D_{Ni} and E_{Ni} , and finally the Zeeman term containing the spin operators and g matrices of two ions.

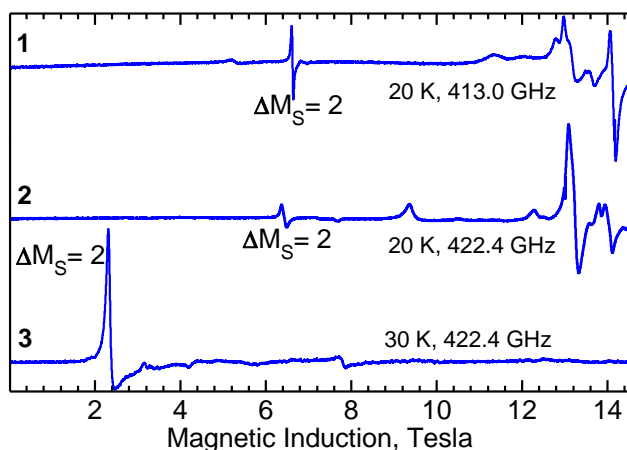


Figure 4. EPR spectra of **1**, **2** and **3** recorded at temperatures and frequencies specified.

$$\hat{H} = J\hat{S}_1\hat{S}_2 + D_{12}\left\{\hat{S}_{z1}\hat{S}_{z2} - \frac{1}{3}\hat{S}_1\hat{S}_2\right\} + E_{12}(\hat{S}_{x1}\hat{S}_{x2} - \hat{S}_{y1}\hat{S}_{y2}) +$$

$$+ D_{Ni1}\left\{\hat{S}_{z1}^2 - \frac{1}{3}S_1(S_1 + 1)\right\} + E_{Ni1}(\hat{S}_{x1}^2 - \hat{S}_{y1}^2) +$$

$$+ D_{Ni2}\left\{\hat{S}_{z2}^2 - \frac{1}{3}S_2(S_2 + 1)\right\} + E_{Ni2}(\hat{S}_{x2}^2 - \hat{S}_{y2}^2) +$$

$$+ \mu_B \mathbf{B}(\{g_{Ni1}\}\hat{S}_1 + \{g_{Ni2}\}\hat{S}_2) \quad (1)$$

The ZFS interaction parameters D_{12} and E_{12} contain the magnetic dipolar and the anisotropic exchange contributions. In complexes **1** and **2**, the nickel atoms are related by the inversion centre ($\frac{1}{2}-x$, $3/2-y$, $1-z$ in **1**; $-x$, $1-y$, $1-z$ in **2**), thus $D_{Ni1} = D_{Ni2}$ and $E_{Ni1} = E_{Ni2}$, and the g matrices of two ions must be also identical, $\{g_{Ni1}\} = \{g_{Ni2}\}$. However, in **3** the two halves of the dinuclear cation are not symmetry-related. The first term in equation (1), the isotropic exchange, gives rise to the eigenstates of the total spin of the system, $\hat{S} = \hat{S}_1 + \hat{S}_2$. In a Ni^{2+} dimer, the total spin S may assume values 0, 1 and 2. The presence of the $S = 1$ and 2 states is best visible in **2** (see Figure 6).

In the strong exchange limit, i.e. when the isotropic exchange interactions are much stronger than the ZFS effects, Hamiltonian (2) may be conveniently expressed using the total spin operator of the system, $\hat{S} = \hat{S}_1 + \hat{S}_2$ (also called the giant spin Hamiltonian). We can write for each spin state S

$$\hat{H}_S = \mu_B \mathbf{B}\{g_S\}\hat{S} + D_S\left\{\hat{S}_z^2 - \frac{1}{3}S(S + 1)\right\} + E_S(\hat{S}_x^2 - \hat{S}_y^2) \quad (2)$$

where the D_S and E_S parameters are different in each spin state S . The transition from Hamiltonian (1) to (2) is accomplished (for the case of two $S = 1$ ions) using equations (3):^{18–21}

$$D_{S=1} = D_{12} - \frac{1}{2}(D_{Ni1} + D_{Ni2})$$

$$D_{S=2} = \frac{1}{3}D_{12} + \frac{1}{6}(D_{Ni1} + D_{Ni2}) \quad (3)$$

The same coupling coefficients relate $E_{S=1}$ and $E_{S=2}$ to E_{Ni} and E_{12} .

In the present cases, the exchange interactions appeared comparable to the ZFS. The exchange integral J magnitude alters the positions of the EPR transitions, while ZFS is dominant. On the other hand, the ZFS parameters affect the magnetic susceptibility, while the J effect prevails (except for **3**). Thus, the EPR and magnetic susceptibility data needed to be treated in a combined iterative procedure. The ZFS parameters were first estimated from the EPR spectra using the “giant spin” Hamiltonian (2). The results were used in the analysis of the magnetic data to determine the J values with help of the microscopic Hamiltonian (1). Next, the EPR spectra were reinterpreted employing the microscopic Hamiltonian (1) with those J values to refine D_{Ni} and E_{Ni} (Figures 5–8). The detailed description of the magnetic studies is given in a later section. A peculiarity of the Ni^{2+} dimers is that the transitions between the $|S, M_S\rangle$ states $|2, 2\rangle \leftrightarrow |2, 1\rangle$ and $|1, -1\rangle \leftrightarrow |1, 0\rangle$, as well as $|2, -2\rangle \leftrightarrow |2, -1\rangle$ and $|1, 1\rangle \leftrightarrow |1, 0\rangle$ overlap when the interaction parameters D_{12} and E_{12} are small compared to D_{Ni} , E_{Ni} . This is so because (neglecting E) the resonance condition for

the $|2, 2\rangle \leftrightarrow |2, 1\rangle$ transition at the Z orientation is $h\nu = g_z\mu_B B + 3D_{S=2}$, while for $|1, -1\rangle \leftrightarrow |1, 0\rangle$ we have $h\nu = g_z\mu_B B - D_{S=1}$, and $D_{S=1} = -3D_{S=2}$ when the interaction contribution is small. Also, the $D_{S=1}$, $E_{S=1}$ are equal to $-D_{Ni}$, $-E_{Ni}$, respectively, under such circumstances.

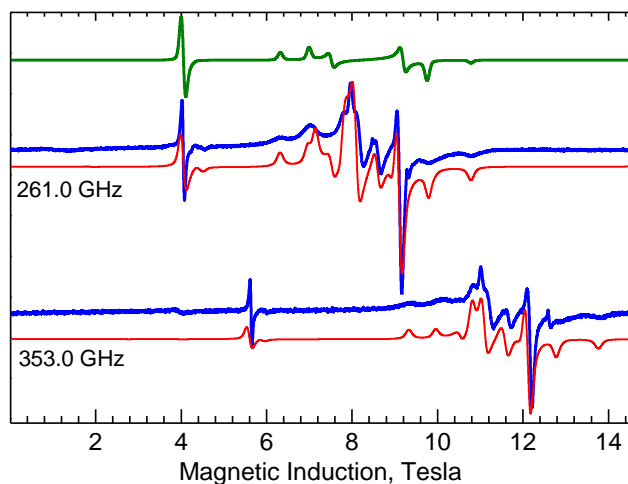


Figure 5. HF EPR spectra of **1**. Blue: experimental recorded at 20 K. Red: simulated with Hamiltonian (1) using $g_x = g_y = 2.21$, $g_z = 2.18$, $D_{Ni1} = D_{Ni2} = 2.27 \text{ cm}^{-1}$, $E_{Ni1} = E_{Ni2} = 0.243 \text{ cm}^{-1}$, $D_{12} = -0.02 \text{ cm}^{-1}$, $E_{12} = 0.04 \text{ cm}^{-1}$, $J = 8.0 \text{ cm}^{-1}$. Green: simulation of the 261 GHz spectrum using the ‘giant spin’ Hamiltonian (2) with $D_{S=1} = -2.27 \text{ cm}^{-1}$, $E_{S=1} = -0.187 \text{ cm}^{-1}$ and g parameters as above. The low-field feature ($\sim 4 \text{ T}$ at 261 GHz, $\sim 5.6 \text{ T}$ at 353 GHz) is the ‘half-field’ transition in the $S = 1$ state.

Broad lines in the spectra of **1** make resolving these transitions impossible, which affects the accuracy of the spin Hamiltonian parameters. Also, the EPR simulation required $J = 8.0 \text{ cm}^{-1}$, rather than 7.7 cm^{-1} as determined from the magnetic data.

The weakly ferromagnetic complex **2** exhibited spectra of mainly $S = 2$ state at lowest temperatures, with the $S = 1$ spectrum emerging at $\sim 15 \text{ K}$ and above (Figures 6 and 7). Thanks

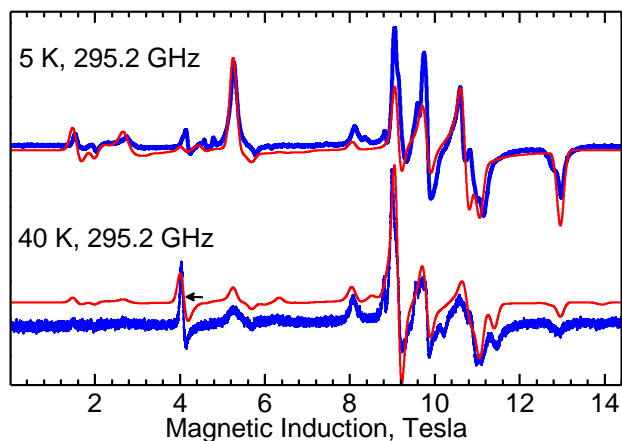


Figure 6. HF EPR spectra of **2**. Blue: experimental. Red: simulated with Hamiltonian (1) using $g_x = g_y = 2.169$, $g_z = 2.200$, $D_{Ni1} = D_{Ni2} = -4.491 \text{ cm}^{-1}$, $E_{Ni1} = E_{Ni2} = -0.684 \text{ cm}^{-1}$, $D_{12} = 0.034 \text{ cm}^{-1}$, $E_{12} = -0.060 \text{ cm}^{-1}$, $J = -6.5 \text{ cm}^{-1}$. The 5 K spectrum is mainly due to the ground $S = 2$ state. A characteristic ‘half-field transition’ in the triplet state ($S = 1$) emerges at elevated temperature near to the magnetic field of 4 T (marked with arrow).

to larger ZFS parameters, the spectra resolution was better than in **1** and the spin Hamiltonian parameters of **2** are more reliable than those of **1**. Interestingly, despite structural similarity to

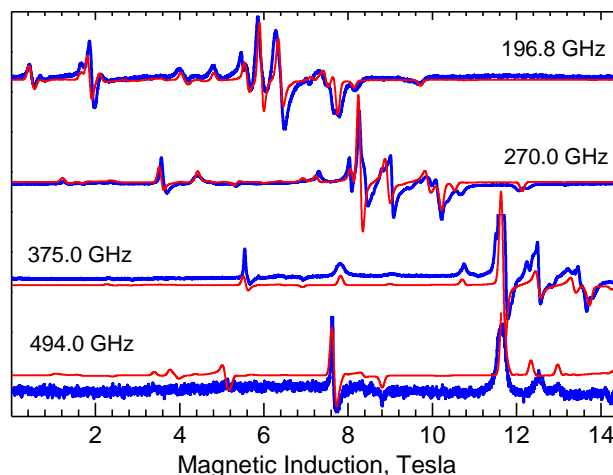


Figure 7. HF EPR spectra of **2**. Blue: experimental, recorded at 20 K and frequencies as indicated. Red: simulated with parameters given in Table 1.

antiferromagnetic **1**, complex **2** is ferromagnetic, has negative D_{Ni} and a pattern of g parameters opposite to that in **1**: $g_{\perp} > g_{\parallel}$ in **1**, but $g_{\perp} < g_{\parallel}$ in **2**. The patterns of g values agree with the sign of D_{Ni} in each case, according to an approximate formula (4),²² while larger $|D|$ in **2** than in **1** is consistent with the more distorted coordination in the former (see section Crystal Structure).

$$D = \lambda (g_z - g_x/2 - g_y/2) / 2 \quad (4)$$

The free-ion spin orbit coupling constant λ for Ni^{2+} is equal to²² -315 cm^{-1} and formula (4) produces D_{Ni} of $+4.7 \text{ cm}^{-1}$ in **1** and -4.7 cm^{-1} in **2**. Formula (4) assumes that only the excited triplet states derived from the ground term 3F contribute to D_{Ni} (see also formulas 5). However, the CASSCF calculations (section Theoretical Calculations) show that states derived from the 1D term also contribute to D_{Ni} .

Complex **3** presents a peculiar case. A prediction of weak antiferromagnetism from the ‘broken symmetry’ DFT calculations is not confirmed by the magnetic data, from which a J value of just -0.6 cm^{-1} was determined (see below). Moreover, when EPR spectra simulation is attempted using the microscopic Hamiltonian (1), one needs to assume J equal to 0. A J value even as small as found from the magnetic data generates features in the simulated spectra which are not observed in experiment. The D_{Ni} magnitude is much larger than in **1** or **2**. Examples of spectra at various temperatures and frequencies are given in Figure 8. Figure 9 shows the frequency dependencies of resonances observed in **3**. Fitting of these dependencies produced the spin Hamiltonian (2) parameters which were used to simulate the powder spectra in Figure 8. Large negative D_{Ni} is again in agreement with the pattern of the g values: $g_{x,y} < g_z$. Formula (4) produces $D_{Ni} = -14.0 \text{ cm}^{-1}$, which is comparable to the experimental value of -11.4 cm^{-1} . The spin Hamiltonian parameters are summarized in Table 1.

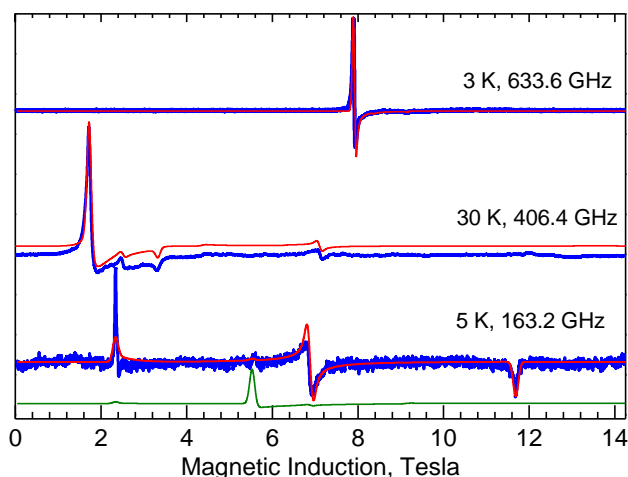


Figure 8. HF EPR spectra of **3**. Blue: experimental, recorded at temperatures and frequencies as indicated. Red: Simulations with $g_x = 2.184$, $g_y = 2.164$, $g_z = 2.263$, $D = -11.398 \text{ cm}^{-1}$, $E = -1.151 \text{ cm}^{-1}$. The green trace was simulated with $D = +11.398 \text{ cm}^{-1}$, $E = +1.151 \text{ cm}^{-1}$ and $\nu = 163.2 \text{ GHz}$. The dominant feature of the 633.6 and 406.4 GHz spectra is the "half-field" $\Delta M_S = 2$ transition, not present at 163.2 GHz.

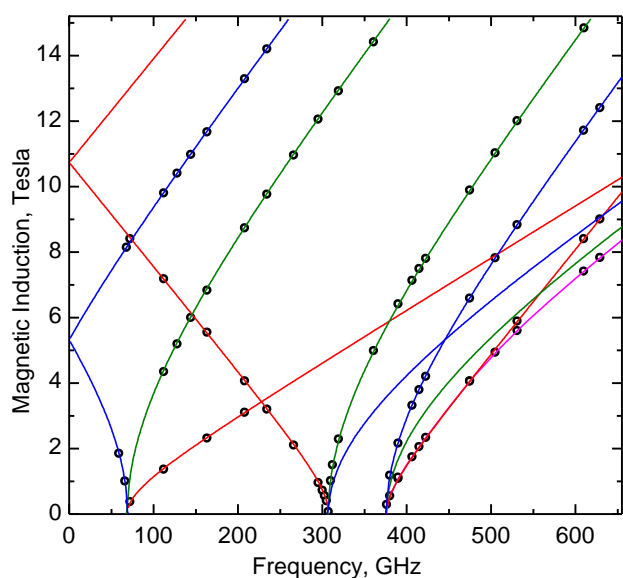


Figure 9. Frequency dependencies of the resonances observed in **3**. The green, blue and red solid lines were calculated at molecular orientations X, Y and Z, respectively, using the spin Hamiltonian parameters given in Table 1. The purple line represents the "half-field" $\Delta M_S = 2$ transition, which is an off-axial feature (not corresponding to X, Y or Z).

Table 1. Spin Hamiltonian parameters used to simulate the HF EPR spectra of **1–3**

	g_x, g_y, g_z	D_{Ni}, D_{12} (cm^{-1})	E_{Ni}, E_{12} (cm^{-1})	J^a (cm^{-1})
1	2.212(6)	2.27(1)	0.245(5)	7.7(2)
	2.212(6)	-0.02(1)	0.04(1)	
	2.181(5)			
2	2.169(3)	-4.491(3)	-0.684(3)	-6.5(2)
	2.169(3)	0.034(4)	-0.060(3)	
	2.200(2)			
3^b	2.184(2)	-11.398(3)	-1.151(3)	-0.6(3)
	2.164(2)	(0)	(0)	
	2.263(4)			

^aFrom magnetic data. ^bGiant spin Hamiltonian (2) was used in EPR simulations.

The Origin of the Spin Hamiltonian Parameters

The g , D and E parameters in transition metal complexes are related to the spin-orbit coupling and ligand field splitting. In hexacoordinated Ni^{2+} complexes with distorted octahedral environment they depend on the ligand-field splitting ${}^3A_g \rightarrow {}^3B_{1g}$, ${}^3A_g \rightarrow {}^3B_{2g}$ and ${}^3A_g \rightarrow {}^3B_{3g}$, using D_{2h} labeling (see Figure 10).

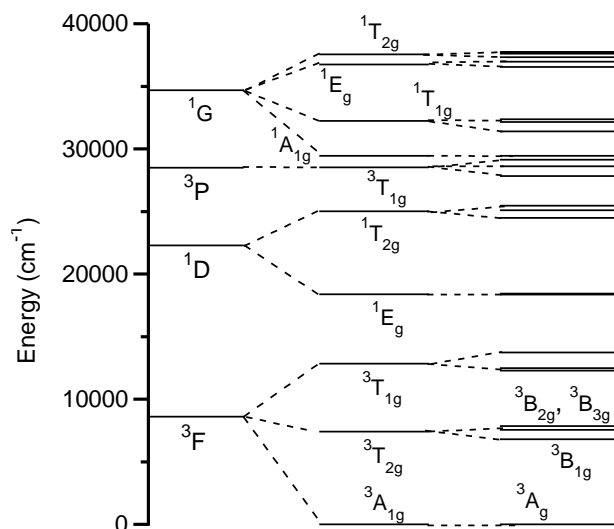


Figure 10. Diagram of the ligand-field states for a Ni^{2+} ion, as calculated for **2** by CASSCF (see Theoretical Calculations below). The calculated energy of the 1S state is 70920 cm^{-1} (not shown). The octahedral T_{2g} , T_{1g} and E_g terms split in the low-symmetry coordination leaving orbitally non-degenerate states (right side of the figure, using D_{2h} labeling).

They are also affected by the anisotropic orbital reduction factor, represented in Formulas 5 by k_x , k_y and k_z . As can be seen in Figure 10, the T_{1g} and T_{2g} terms of O_h split in the actual low symmetry into a pair of close levels and one more distant, which is close to the situation of the D_{4h} symmetry, where these pairs of close levels would be degenerate forming an E_g term. The ${}^3B_{2g}$ and ${}^3B_{3g}$ levels, which appear in Formulas 5, come from the 3E_g term in D_{4h} symmetry.

$$g_x = g_e - \frac{8\lambda k_x^2}{E({}^3B_{2g}) - E({}^3A_g)}$$

$$g_y = g_e - \frac{8\lambda k_y^2}{E({}^3B_{3g}) - E({}^3A_g)}$$

$$g_z = g_e - \frac{8\lambda k_z^2}{E({}^3B_{1g}) - E({}^3A_g)} \quad (5)$$

$$D_{Ni} = -2\lambda^2 \left(\frac{2k_z^2}{E({}^3B_{1g}) - E({}^3A_g)} - \frac{k_x^2}{E({}^3B_{2g}) - E({}^3A_g)} - \frac{k_y^2}{E({}^3B_{3g}) - E({}^3A_g)} \right)$$

It is noteworthy that the energy sequence in **2**, ${}^3B_{1g} < ({}^3B_{2g} \approx {}^3B_{3g})$ is reversed in **1** to $({}^3B_{3g} \approx {}^3B_{2g}) < {}^3B_{1g}$ (see Tables S5-S7), and this results in positive D_{Ni} in **1** and reversal of the g pattern as described above (see Table 1).

Magnetic studies

The results of magnetic susceptibility measurements of **1–3** are given in Figure 11 in the form χT versus T (χ is the corrected molar magnetic susceptibility per one Ni(II) ion and T is absolute temperature). At higher temperatures, complexes **1–3** behave similarly; the room temperature χT values are above $2 \text{ cm}^3 \text{ K mol}^{-1}$ corresponding to the presence of two Ni^{2+} ions. These values strongly decrease (**1** and **3**) or increase (**2**) below 50 K. The behavior of **2** is characteristic of ferromagnetic coupling and that of **1** indicates antiferromagnetic coupling. While the χT plot of **3** seems to be similar to that of **1**, the decrease of χT at low temperatures in **3** is caused by large zero-field splitting on each Ni^{2+} ion rather than by the exchange interactions.

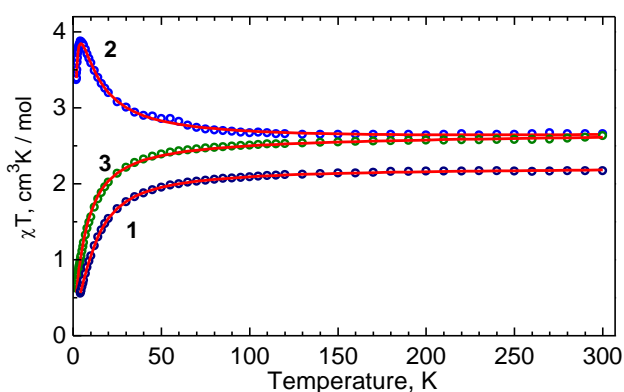


Figure 11. The product of the magnetic susceptibility and temperature, χT as a function of temperature. The temperature independent paramagnetism (TIP) contribution was subtracted. The original magnetic data are given in Figure S5. Red lines were calculated using parameters in Table 1.

The three complexes exhibit moderate (**1**) to very large (**3**) zero-field splitting whose magnitude is comparable to kT at low temperatures, thus affecting the magnetic properties. In studies on dimeric complexes, the well-known Bleaney–Bowers type equation²³ is typically used:

$$\chi_{dim} = \frac{Ng^2\mu_B^2 \sum_S (2S+1)(S+1) S e^{-\frac{JS(S+1)}{2kT}}}{3kT \sum_S (2S+1) e^{-\frac{JS(S+1)}{2kT}}} + 2TIP \quad (6)$$

where the summation runs over the states of the Heisenberg–Dirac–VanVleck Hamiltonian $\hat{H} = J\hat{S}_1 \cdot \hat{S}_2$ ($S = 0, 1$ and 2 here). Equation (6) relies on J being much larger than both the Zeeman and zero-field splitting. Since this is not the case here, the magnetic susceptibility must be calculated from the fundamental formula

$$\chi_{dim} = -\frac{N \sum_i \frac{\partial E_i}{\partial B} e^{-\frac{E_i}{kT}}}{\sum_i e^{-\frac{E_i}{kT}}} + 2TIP \quad (7)$$

where the summation runs over all 9 $|M_{S1}, M_{S2}\rangle$ states in the Ni–Ni system. The energies E_i were determined by diagonalizing the spin Hamiltonian (1) matrix. The $\partial E_i / \partial B$ derivatives were calculated numerically, by evaluating energies E_i 5 Gauss below and 5 Gauss above the magnetic field of the the SQUID instrument (5000 G). Formula (7) gives magnetic susceptibility $\chi(\Theta, \Phi)$ at an orientation of a molecule versus the magnetic field and needs still to be averaged over all orientations, which is accomplished by numerical integration of $\chi(\Theta, \Phi) \sin\Theta d\Theta d\Phi$. In the fitting procedure, the D_{Ni} , E_{Ni} and D_{12} , E_{12} parameters were fixed as obtained from EPR. The fitted J values are given in Table 2 together with the ZFS parameters, and complete fitting results are provided in Table S4.

Table 2. Experimental and calculated exchange and zero-field splitting parameters

	D_{Niexp}^a cm^{-1}	D_{Nicalc}^b cm^{-1}	E_{Niexp}^a cm^{-1}	E_{Nicalc}^b cm^{-1}	J_{exp}^c cm^{-1}	J_{calc}^d cm^{-1}
1	2.27(1)	1.2	0.243(5)	0.18	7.7(2)	7.2
2	-4.491(3)	-7.2	-0.684(3)	-0.80	-6.5(2)	-17
3^e	-11.398(5)	-10.8	-1.151(5)	-2.50	-0.6(3)	7.5
		-13.3		-3.6		

^aDetermined from EPR. ^bCASSCF calculation. ^cFrom magnetic data. ^dBroken symmetry calculation. ^eTwo inequivalent Ni ions are present but only one EPR spectrum was observed.

Theoretical Calculations

Quantum mechanical software package ORCA²⁴ was employed in calculations of the zero-field splitting and exchange integrals in **1–3**. The X-Ray coordinates were used. Optimizing the hydrogen atom positions, which is sometimes recommended, had no significant effect. The ZFS parameters D_{Ni} and E_{Ni} were calculated using the CASSCF method²⁵ with 8 electrons in 5 orbitals. All 10 triplet states and 15 singlet states were taken into account. The initial guesses were provided by calculations based on the B3LYP functional in conjunction with the def2-TZVPP²⁶ functions for Ni and all coordinated atoms and TZVPP²⁷ functions for the remaining atoms. In the zero-field splitting calculations, one of the Ni atoms in the structure was replaced by Zn. Relatively recent literature data²⁸ indicate that the NEVPT2 method does not produce for Ni^{2+} better ZFS parameters than CASSCF does, thus it was not attempted here. The exchange coupling constants J between the Ni^{2+} ions were calculated using the “broken symmetry” approach,^{29–37} as implemented in ORCA. These J values were determined by taking the difference of the SCF energies calculated for the high-spin state ($S = 2$) and the broken-symmetry ($S = 0$) state. The BS state corresponds to configurations in which two unpaired spin-up, α electrons are localized on one site and two unpaired spin-down, β electrons localized on the other site. The J values (using the $\hat{H} = J\hat{S}_1 \cdot \hat{S}_2$ formalism) were evaluated by means of the $J = 2(\epsilon_{HS} - \epsilon_{BS}) / (\langle \hat{S}^2 \rangle_{HS} - \langle \hat{S}^2 \rangle_{BS})$ expression,

where ϵ are the energies and $\langle \hat{S}^2 \rangle$ are the average values of the total spin-squared operator in the HS and BS states.

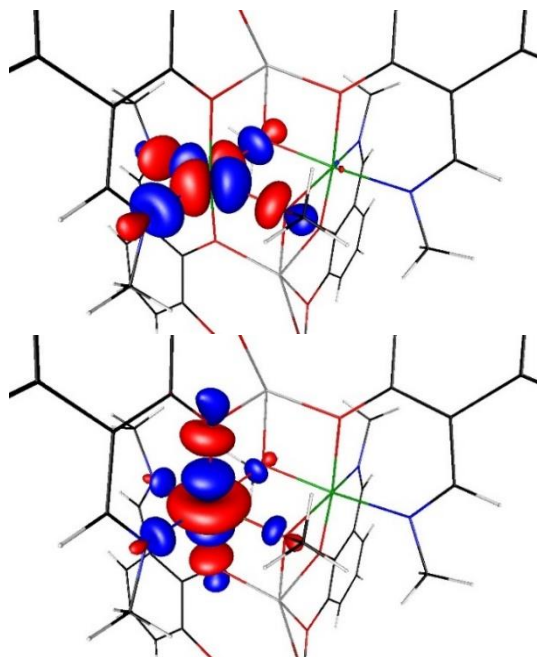


Figure 12. The magnetic orbitals (corresponding orbitals, “uco”, in ORCA) of one Ni^{2+} ion in **1**. Orbitals of identical shape exist on the other Ni^{2+} ion. The overlap integrals are 0.068 and 0.013 for the corresponding orbitals of the $d_{x^2-y^2}$ (top) and d_{z^2} type (bottom), respectively. The isosurfaces were plotted at the 0.04 value (red) and -0.04 (blue). The outer parts of the molecule are cut-off.

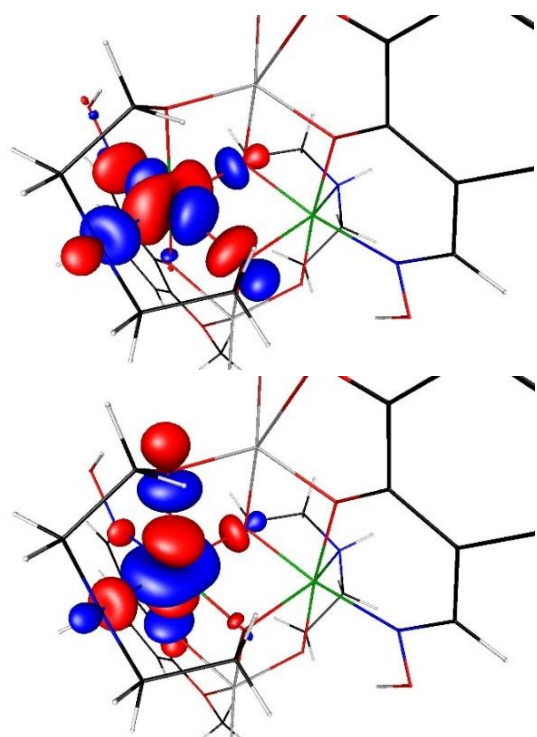


Figure 13. The magnetic orbitals of one Ni^{2+} ion in **2**. The overlap integrals are 0.040 and 0.010 for the corresponding orbitals on top and at bottom, respectively. The outer parts of the molecule are cut-off.

The calculations reproduced the trends in the D_{Ni} and J values while the quantitative results were rather poor. This is less surprising in the case of the ZFS, but the J values calculated from the “broken symmetry” formalism were distant from the experimental values for **2** and **3** (Table 2). This is disappointing, as in the experience of present authors, broken symmetry calculations tend to produce J overestimated by up to 50%. The magnitude and sign of the exchange interactions is determined by the overlap of the metal orbitals of two ions containing the unpaired electrons. Increasing overlap integral results in larger antiferromagnetic contribution to the isotropic exchange interactions. In the case of Ni^{2+} , there are two orbitals containing unpaired electrons. For **1**, the two overlap integrals are 0.068 and 0.013 for the orbitals having mainly $d_{x^2-y^2}$ and d_{z^2} character, respectively (Figure 12). For **2**, the corresponding numbers are 0.040 and 0.010 (Figure 13). The overlaps depend on the geometry of a dimer and it is known that the increasing Me–O–Me bridge angle favors the antiferromagnetism of a dimeric compound.³⁸ In **1** and **2** the NiONi angles are 100.5° and 98.3°, respectively. Complex **3** is not comparable to **1** or **2**, as it has only a single bridge, with the NiONi angle of 125° and seems to exhibit no metal–metal interactions despite the results of the broken symmetry calculations (Figure 14).

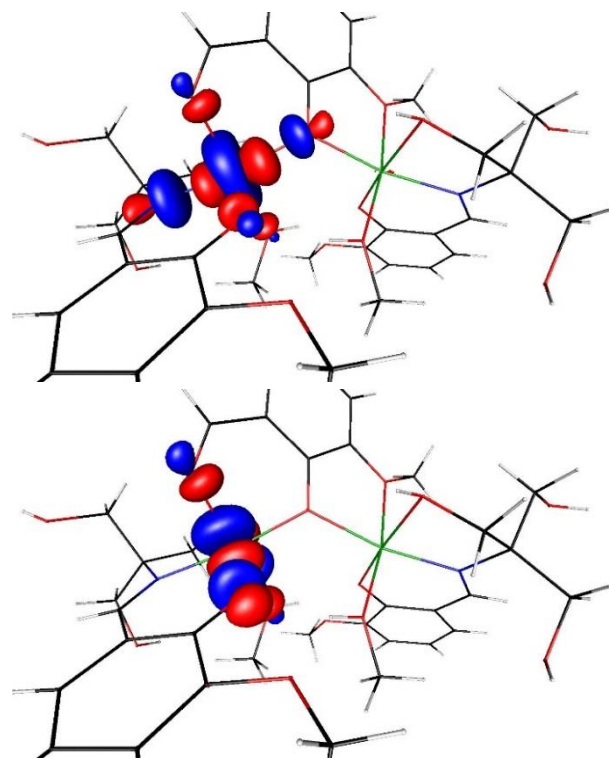


Figure 14. The magnetic orbitals in **3**.

The CASSCF calculations reproduce the sign of the D_{Ni} parameter as well as its trend among the three compounds (Table 2). The most important contributions to D are listed in Table 3 and complete listings are provided in Tables S5–S7. For **1**, there were 3 large contributions to D_{Ni} due to the lowest excited triplet states and three large contributions due to the

excited singlet states, however the latter ones nearly cancel each other out. The overall contribution of the triplet states was 1.43 cm^{-1} , while that of the singlet states was -0.17 cm^{-1} . Similar relations were observed for **2**, with three triplet and three singlet states contributing -9.2 and 0.89 cm^{-1} , respectively. The very large D_{Ni} in **3** consists mainly of three triplet components contributing -13.75 cm^{-1} and three singlet-related components whose sum is 1.79 cm^{-1} . These relations indicate that the classical formulas 4 and 5, in which only three lowest excited triplet states, derived from the ${}^4\text{T}_{2g}({}^4\text{F})$ term in O_h symmetry, are taken into account, are reasonable approximations. For **1** and **2**, there are essentially no significant contributions other than those in Table 3, while in the case of **3** more excited states affect the zero-field splitting, including states derived from the ${}^1\text{T}_{2g}({}^1\text{G})$ and ${}^1\text{E}_g({}^1\text{G})$ terms (Table S7). As is seen, the ZFS parameters are small sums of large numbers of alternating sign, which explains the difficulty of reproducing them quantitatively.

Table 3. The largest contributions to D from the CASSCF excited states

Parent state in O_h	1		2		3	
	Energy ¹ cm^{-1}	D cm^{-1}	Energy ¹ cm^{-1}	D cm^{-1}	Energy ¹ cm^{-1}	D cm^{-1}
${}^3\text{T}_{2g}({}^3\text{F})$	7619	13.385	6675	-47.001	6555	-64.497
	7670	11.544	6819	13.555	6690	26.721
	7766	-23.483	6877	24.245	6749	24.030
${}^1\text{T}_{2g}({}^1\text{D})$	25465	-7.282	24404	15.188	24448	15.660
	25512	-7.270	24984	-7.152	25536	-7.119
	25612	14.384	25340	-7.144	26349	-6.453

¹The energies include the spin-orbit coupling contribution. Energies of pairs of close levels are printed in boldface.

Conclusions

The generation of the Schiff base ligands *in situ* along with the use of a zerovalent metal (Ni and Zn in **1**, Zn only in **2** and **3**) afforded the reaction systems with complex equilibria between several components that eventually produced **1**, **2** and **3** as the most stable assemblies. The first two complexes are symmetric dimers with a $\text{Ni}_2\text{Zn}_2\text{O}_6$ central core and Ni...Ni distances of 3.220 and 3.146 Å, respectively. The third compound is a novel heterometallic cocrystal salt solvate built of alternating sheets of a neutral zwitterionic Zn^{II} Schiff base complex and of ionic salt containing dinuclear Ni^{II} complex cations. The phenolate-bridged Ni atoms in cation of **3** are separated by 3.33 Å. The cation lacks crystallographic symmetry. Thanks to the HFEP, the zero-field splitting parameters D_{Ni} and E_{Ni} were determined in all three cases. The CASSCF calculations reproduced the trend and signs of the D_{Ni} parameters. "Broken symmetry" calculations on **1** and **2** confirmed the known relation between the MOM angle in doubly-bridged MOOM systems and the type of magnetism – antiferromagnetism is favored for larger angles due to increased overlap of magnetic orbitals. Complex **3** represents a special combination of structural features that include a single bridge and an asymmetric obtuse NiONi angle,

and much larger ZFS compared to that of **1** and **2**. The decrease of χT at low temperatures in **3** is caused by large zero-field splitting on each Ni^{2+} ion rather than by antiferromagnetic coupling despite the results of the broken symmetry calculations.

Experimental

Reagents and General Procedures

o-Vanillin was purchased from Aldrich and used as received. All other chemicals were purchased from local suppliers and used without further purification. All solvents were of AP-grade. All the experiments were carried out in air. Elemental analyses for C, H, N were performed with a Perkin-Elmer 2400 analyzer. Infrared (IR) spectra were recorded on a Perkin-Elmer 1600 FT-IR spectrometer from a KBr pellet in the 400–4000 cm^{-1} region (Figures S3–S5).

Synthesis of $[\text{NiZnL}'_2(\text{OMe})\text{Cl}]_2$ (1**).** *o*-Vanillin (0.15 g, 1 mmol) in 5 mL ethanol was magnetically stirred with $\text{CH}_3\text{NH}_2\cdot\text{HCl}$ (0.07 g, 1 mmol) and diethanolamine (0.2 mL) in a 50 mL conical flask at 333 K for 15 min. Next, Ni and Zn powders (0.03 g, 0.5 mmol both) accompanied by NH_4I (0.07 g, 0.5 mmol) were added to the resulting yellow solution of the Schiff base. The mixture that gradually turned dark-green was kept stirring for 3 h at 333 K until dissolution of the metal powders was achieved (adhesion of a small fraction of nickel particles to the stirring bar precluded complete dissolution of the metal). The resultant solution was filtered and left to stand at room temperature. Successive addition of Pr^iOH (6 ml) in three portions over a month's time did not induce crystallization. The solution was evaporated to dryness in air, and the residue was redissolved in 3 ml methanol. Pale green plate-like crystals of **1** suitable for X-ray diffraction were formed by the following day. They were filtered off, washed with dry Pr^iOH and dried in air. Yield: 63%. Anal. Calcd for $\text{C}_{38}\text{H}_{46}\text{Cl}_2\text{N}_4\text{Ni}_2\text{O}_{10}\text{Zn}_2$ (1037.865): C 43.98, H 4.47, N 5.40%. Found: C 43.67, H 4.24, N 5.52%. IR (ν/cm^{-1}): 3450, 3060, 2922, 2814, 1682, 1640, 1602, 1434, 1402, 1310, 1248, 1222, 1170, 1148, 1082, 1050, 1008, 972, 860, 784, 736, 636, 545, 490.

Synthesis of $[\text{NiZnL}''(\text{Dea})\text{Cl}]_2\cdot 2\text{DMF}$ (2**).** *o*-Vanillin (0.15 g, 1 mmol), $\text{NH}_2\text{OH}\cdot\text{HCl}$ (0.07 g, 1 mmol), diethanolamine (0.5 mL) and 15 mL DMF in a 50 mL conical flask were magnetically stirred at 333 K for 30 min. $\text{NiCl}_2\cdot 6\text{H}_2\text{O}$ (0.24 g, 1 mmol) dissolved in 5 mL ethanol was added to the flask and the solution was stirred at the same temperature for another 30 min. After that, Zn powder (0.06 g, 1 mmol) was added and the mixture was kept stirring until total dissolution of the zinc powder was observed (1 h). The resultant green solution was filtered and left to stand at room temperature. Blue plate-like crystals of **2** suitable for X-ray diffraction were formed over several days. They were filtered off, washed with dry Pr^iOH and dried in air. Yield: 71%. Anal. Calcd for $\text{C}_{30}\text{H}_{48}\text{Cl}_2\text{N}_6\text{Ni}_2\text{O}_{12}\text{Zn}_2$ (1003.81): C 35.90, H 4.82, N 8.37%. Found: C 35.75, H 4.98, N 8.05%. IR (ν/cm^{-1}): 3410, 3398, 3384, 3280, 2942, 2892, 2838, 1636, 1552,

1468, 1446, 1416, 1374, 1300, 1244, 1216, 1172, 1080, 1044, 960, 854, 786, 742, 654, 626, 576, 440.

Synthesis of $[\text{Ni}_2(\text{H}_3\text{L}''')_2(\text{o-Van})(\text{MeOH})_2]\text{Cl}\cdot[\text{ZnCl}_2(\text{H}_4\text{L}''')(\text{MeOH})]\cdot 2\text{MeOH}$ (**3**). *o*-Vanillin (0.30 g, 2 mmol) and tris (0.24 g, 2 mmol) were added to methanol (20 ml) and stirred magnetically for 30 min. Next $\text{NiCl}_2\cdot 6\text{H}_2\text{O}$ (0.24 g, 1 mmol) and zinc powder (0.06 g, 1 mmol) were added to the yellow solution and the mixture was heated to 323 K under stirring until total dissolution of the zinc powder was observed (1 h). The resulting green solution was filtered and allowed to stand at room temperature. Bright-green rods of the title compound were formed within several days. They were collected by filter-suction, washed with dry Pr^iOH and finally dried in air (yield: 68% based on zinc). Anal. Calcd for $\text{C}_{49}\text{H}_{76}\text{Cl}_3\text{N}_3\text{Ni}_2\text{O}_{23}\text{Zn}$ (1364.26): C, 43.14; H, 5.61; N, 3.08%. Found: C, 42.92; H, 5.45; N, 3.37%. IR (ν/cm^{-1}): 3410, 3384, 3280, 3074, 3014, 2942, 2892, 2838, 1636, 1610, 1552, 1468, 1446, 1416, 1300, 1244, 1216, 1172, 1080, 1044, 976, 960, 854, 786, 742, 654, 608, 576, 530.

Crystal Structure Determination

The crystal data for **1**, **2** and **3** are summarized in Table S4, selected coordination geometries are given in Tables S1 and S2 with hydrogen bonding geometries for **3** listed in Table S8. Crystallographic data for the structures were collected at 100(2) K for **1** and **3** and 180(2) K for **2** on an Oxford Diffraction Gemini diffractometer fitted with Cu $\text{K}\alpha$ (**1**, **3**) or Mo $\text{K}\alpha$ (**2**) radiation. Following semi-empirical from equivalents (**1**) or analytical absorption corrections (**2**, **3**) and solution by direct methods, the structures were refined against F^2 with full-matrix least-squares using the program SHELXL-97 and SHELXL-2017.³⁹ The assignments of the metal atom for the Ni and Zn sites were based on refinement and considerations of coordination geometries. There was no evidence of any Zn mixing with the Ni sites. All the hydroxyl hydrogen atoms in **3** were located and refined with O-H distances restrained to ideal values. All remaining hydrogen atoms were added at calculated positions and refined by use of a riding model with isotropic displacement parameters based on those of the parent atom. Anisotropic displacement parameters were employed for the non-hydrogen atoms.

Magnetic measurements

Magnetic susceptibility measurements of powdered samples over the temperature range 1.8–300 K at the magnetic field of 5000 G were carried out with a SQUID magnetometer (Quantum Design MPMSXL-5). Corrections for the sample holders were applied. Diamagnetic corrections for the molecule were determined from Pascal constants.⁴⁰ The original magnetic data are given in Figure S6.

High-Field Spectroscopy

HF-EPR spectra of powdered samples of **1–3** were recorded using a home-built spectrometer at the EMR facility of NHMFL.⁴¹ The instrument is a transmission-type device in which

waves are propagated in cylindrical lightpipes. The microwaves were generated by a phase-locked oscillator (Virginia Diodes) operating at a frequency of 13 ± 1 GHz and generating its harmonics, of which the 4th, 8th, 16th, 24th, 32nd and 48th were available. A superconducting magnet (Oxford Instruments) capable of reaching a field of 17 T was employed.

Authors contribution

Study concept and design: O.Yu. Vassilyeva; acquisition of data: E.A. Buvaylo (synthesis), B.W. Skelton and A.N. Sobolev (X-ray crystallography), A. Bieńko (magnetic measurements), A. Ozarowski (HF EPR spectra); analysis and interpretation of data: O.Yu. Vassilyeva (synthetic and structural data) and A. Ozarowski (EPR and magnetic data); theoretical calculations: A. Ozarowski; drafting and revising of the manuscript: O.Yu. Vassilyeva and A. Ozarowski; study supervision: V.N. Kokozay.

Conflicts of interest

There are no conflicts to declare.

Acknowledgements

Funding for this research was provided by Ministry of Education and Science of Ukraine (grant No. 19BF037-05). A portion of this work was performed at the National High Magnetic Field Laboratory, which is supported by National Science Foundation Cooperative Agreement No. DMR-1644779 and the State of Florida.

References

- C. E. Valdez, Q. A. Smith, M. R. Nechay and A. N. Alexandrova, *Acc. Chem. Res.*, 2014, **47**, 3110.
- (a) M. J. Maroney and S. Ciurli, *Chem. Rev.*, 2014, **114**, 4206; (b) T. Cheng, H. Li, W. Xia, L. Jin and H. Sun, *Coord. Chem. Rev.*, 2016, **311**, 24.
- R. Bythell-Douglas, U. Suttisansanee, G. R. Flematti, M. Challenor, M. Lee, S. Panjikar, J. F. Honek and C. S. Bond, *Chem.–Eur. J.*, 2015, **21**, 541.
- (a) S. Hematian, I. Garcia-Bosch and K. D. Karlin, *Acc. Chem. Res.*, 2015, **48**, 2462; (b) S. Gao, Y. Liu, Y. Shao, D. Jiang and Q. Duan, *Coord. Chem. Rev.*, 2020, **402**, 213081.
- C. Benelli and D. Gatteschi, *Introduction to Molecular Magnetism – From Transition Metals to Lanthanides*. Weinheim: Wiley-VCH, 2015.
- J. M. Frost, K. L. Harriman and M. Murugesu, *Chem. Science*, 2016, **7**, 2470.
- C. Cadiou, M. Murrie, C. Paulsen, V. Villar, W. Wernsdorfer and R. E. Winpenny, *ChemComm*, 2001, 2666.
- S. T. Ochsenein, M. Murrie, E. Rusanov, H. Stoeckli-Evans, C. Sekine and H. U. Güdel, *Inorg. Chem.*, 2002, **41**, 5133.
- (a) E. Colacio, J. Ruiz, A. J. Mota, M. A. Palacios, E. Cremades, E. Ruiz, F. J. White and E. K. Brechin, *Inorg. Chem.* 2012, **51**, 5857; (b) H.-R. Wen, S.-J. Liu, X.-R. Xie, J. Bao, C.-M. Liu and J.-L. Chen, *Inorg. Chim. Acta*, 2015, **435**, 274.
- (a) O. V. Nesterova, E. N. Chygorin, V. N. Kokozay, V. V. Bon, I. V. Omelchenko, O. V. Shishkin, J. Titiš, R. Boča, A. J. Pombeiro and A. Ozarowski, *Dalton Trans.*, 2013, **42**, 16909; (b) O. V.

- Nesterova, E. N. Chygorin, V. N. Kokozay, I. V. Omelchenko, O. V. Shishkin, R. Boča and A. J. Pombeiro, *Dalton Trans.*, 2015, **44**, 14918; (c) O. V. Nesterova, K. V. Kasyanova, V. G. Makhankova, V. N. Kokozay, O. Y. Vassilyeva, B. W. Skelton, D. S. Nesterov and A. J. L. Pombeiro, *Appl. Catal. A Gen.*, 2018, **560**, 171; (d) O. V. Nesterova, K. V. Kasyanova, E. A. Buvaylo, O. Yu. Vassilyeva, B. W. Skelton, D. S. Nesterov and A. J. L. Pombeiro, *Catalysts*, 2019, **9**, 209; (e) V. N. Kokozay, O. Y. Vassilyeva and V. G. Makhankova, In *Direct Synthesis of Metal Complexes*, ed. B. Kharisov, Elsevier: Amsterdam, 2018.
- 11 E. Grothe, H. Meekes, E. Vlieg, J. H. Ter Horst and R. De Gelder, *Cryst. Growth Des.*, 2016, **16**, 3237.
- 12 (a) A. Jana, T. Weyhermüller and S. Mohanta, *CrystEngComm*, 2013, **15**, 4099; (b) S. Sarkar and S. Mohanta, *RSC Adv.*, 2011, **1**, 640; (c) A. Cucos, A. Ursu, A. M. Madalan, C. Duhayon, J.-P. Sutter and M. Andruh, *CrystEngComm*, 2011, **13**, 3756; (d) S. Hazra, P. Chakraborty and S. Mohanta, *Cryst. Growth Des.*, 2016, **16**, 3777; (e) S. Hazra, R. Meyrelles, A. J. Charmier, P. Rijo, M. F. da Silva and A. J. L. Pombeiro, *Dalton Trans.*, 2016, **45**, 17929; (f) N. Hari, A. Jana and S. Mohanta, *Inorg. Chim. Acta*, 2017, **467**, 11.
- 13 J. Krzystek, S. A. Zvyagin, A. Ozarowski, S. Trofimenko and J. Telsler, *J. Magn. Reson.* 2006, **178**, 174.
- 14 (a) R. Herchel, R. Boča, J. Krzystek, A. Ozarowski, M. Durán and J. van Slageren, *J. Am. Chem. Soc.*, 2007, **129**, 10306; (b) H. Sakiyama, Y. Chiba, K. Tone, M. Yamasaki, M. Mikuriya, J. Krzystek and A. Ozarowski, *Inorg. Chem.*, 2016, **56**, 138.
- 15 (a) O. Yu. Vassilyeva, N. D. Nevesenko, V. V. Skopenko, Yu. S. Gerasimenko and V. N. Kokozay, *Dopov. Akad. Nauk Ukr. RSR*, Ser. B, 1988, 36; (b) O. Yu. Vassilyeva and V. N. Kokozay, *Ukr. Khim. Zh. (Russ. Ed.)*, 1993, **59**, 176; (c) V. N. Kokozay, O. Yu. Vassilyeva and V. A. Pavlenko, In *Direct Synthesis of Coordination and Organometallic Compounds*, ed. A. D. Garnovskii and B. I. Kharissov, Elsevier Science: Amsterdam, 1999; (d) E. A. Buvaylo, O. V. Nesterova, V. N. Kokozay, O. Yu. Vassilyeva, B. W. Skelton, R. Boča and D. S. Nesterov, *Cryst. Growth Des.*, 2012, **12**, 3200; (e) E. A. Buvaylo, V. N. Kokozay, O. Yu. Vassilyeva, B. W. Skelton, I. L. Eremenko, J. Jezierska and A. Ozarowski, *Inorg. Chem.*, 2009, **48**, 11092.
- 16 (a) E. A. Buvaylo, O. Yu. Vassilyeva, B. W. Skelton, *Acta Cryst.*, 2015, **E71**, 1307; (b) E. A. Buvaylo, O. Yu. Vassilyeva, B. W. Skelton, *Acta Cryst.*, 2015, **E71**, 1203.
- 17 A. Tarai and J. B. Baruah, *CrystEngComm*, 2016, **18**, 5482.
- 18 A. Bencini, D. Gatteschi, In *EPR of Exchange Coupled Systems*; Springer Verlag: Berlin/Heidelberg, 1990; (b) A. Abragam, B. Bleaney, In *Electron Paramagnetic Resonance of Transition Ions*; Clarendon Press: London, 1970; (c) J. Owen, *J. Appl. Phys.*, 1961, **32**, S213; (d) R. Boča, In *Theoretical Foundations of Molecular Magnetism*; Elsevier: Amsterdam, 1999; (e) R. Boča, *Coord. Chem. Rev.*, 2004, **248**, 757.
- 19 (a) V. V. Semenaka, O. V. Nesterova, V. N. Kokozay, V. V. Dyakonenko, R. I. Zubatyuk, O. V. Shishkin, R. Boča, J. Jezierska, A. Ozarowski, *Inorg. Chem.*, 2010, **49**, 5460; (b) H. Riesen, H. U. Gudel, *Mol. Phys.*, 1987, **60**, 1221; (c) T. J. Morsing, H. Weihe, J. Bendix, *Inorg. Chem.*, 2016, **55**, 1453; (d) J. Glerup, P. Goodson, D. J. Hodgson, M. Athar Masood, K. Michelsen, *Inorg. Chim. Acta*, 2005, **358**, 295.
- 20 (a) M. Y. Okamura, B. M. Hoffman, *J. Chem. Phys.*, 1969, **51**, 3128; (b) A. Ozarowski, B. R. McGarvey, J. E. Drake, *Inorg. Chem.*, 1995, **34**, 5558; (c) S. J. W. Holgate, G. Bondarenko, D. Collison, F. E. Mabbs, *Inorg. Chem.*, 1999, **38**, 2380; (d) P. ter Heerdt, M. Stefan, E. Goovaerts, A. Caneschi, A. Cornia, *J. Magn. Reson.*, 2006, **179**, 29.
- 21 B. L. Tran, J. Krzystek, A. Ozarowski, C.-H. Chen, M. Pink, J. A. Karty, J. Telsler, K. Meyer, D. J. Mindiola, *Eur. J. Inorg. Chem.*, 2013, 3916.
- 22 R. Boča, *Struct. Bond.*, 2006, **117**, 1.
- 23 B. Bleaney, K. D. Bowers, *Proc. Roy. Soc. A*, 1952, **214**, 451.
- 24 (a) F. Neese, *ORCA - An Ab Initio, Density Functional and Semiempirical Program Package*, Version 4.0.1; Surf Sara: Amsterdam, 2017; (b) F. Neese, The ORCA Program System. *Wiley Interdiscip. Rev. Comput. Mol. Sci.*, 2012, **2**, 73.
- 25 (a) B. O. Roos, P. R. Taylor, P. E. M. Sigbahn, *Chem. Phys.*, 1980, **48**, 157; (b) C. Angeli, C. R. Cimraglia, S. Evangelisti, T. Leininger, J.-P. Marlieu, *J. Chem. Phys.*, 2001, **114**, 10252; (c) F. Neese, *J. Chem. Phys.*, 2007, **127**, 164112.
- 26 (a) K. Eichkorn, O. Treutler, H. Öhm, M. Häser, R. Ahlrichs, *Chem. Phys. Lett.*, 1995, **240**, 283; (b) The Ahlrichs auxiliary basis sets (<https://www.basissetexchange.org/>) have been hardwired into the ORCA software.
- 27 (a) A. Schäfer, H. Horn, R. Ahlrichs, *J. Chem. Phys.*, 1992, **97**, 2571; (b) Ahlrichs, R; *et al.*, unpublished.
- 28 G. Novitchi, S. Jiang, S. Shova, F. Rida, I. Hlavička, M. Orlita, W. Wernsdorfer, R. Hamze, C. Martins, N. Suaud, N. Guihéry, A. L. Barra, C. Train, *Inorg. Chem.*, 2017, **56**, 14809.
- 29 A. D. Becke, *Phys. Rev. A*, 1988, **38**, 3098.
- 30 J. P. Perdew, *Phys. Rev. B*, 1986, **33**, 8822.
- 31 J. P. Perdew, *Phys. Rev. B*, 1986, **34**, 7406.
- 32 L. Noodleman, *J. Chem. Phys.*, 1981, **74**, 5737.
- 33 L. Noodleman, E. R. Davidson, *Chem. Phys.*, 1986, **109**, 131.
- 34 L. Noodleman, D. A. Case, *Adv. Inorg. Chem.*, 1992, **38**, 423.
- 35 J. P. Malrieu, R. Caballol, C. J. Calzado, C. de Graaf, N. Guihéry, *Chem. Rev.*, 2014, **114**, 429.
- 36 N. Onofrio, J.-M. Mouesca, *Inorg. Chem.*, 2011, **50**, 5577.
- 37 A. Rodríguez-Fortea, P. Alemany, S. Alvarez, E. Ruiz, *Inorg. Chem.*, 2002, **41**, 3769.
- 38 E. Ruiz, P. Alemany, S. Alvarez, J. Cano, *J. Am. Chem. Soc.*, 1997, **119**, 1297.
- 39 G.M. Sheldrick, *Acta Cryst. C*, 2015, **71**, 3.
- 40 (a) E. König, In *Magnetic Properties of Coordination and Organometallic Transition Metal Compounds*; edited by Hellwege, K.-H., Hellwege, A. M., pp. 27–29; Springer, Berlin, 1966; (b) G. A. Bain, J. F. Berry, *J. Chem. Educ.*, 2008, **85**, 532.
- 41 A. Hassan, L. Pardi, J. Krzystek, A. Sienkiewicz, P. Goy, M. Rohrer, L.-C. Brunel, *J. Magn. Reson.*, 2000, **142**, 300.